BER the international journal of bridge engineering management and research

Real-Time Risk Assessment of Bridges Subject To Storm-Induced Scour

Neandro DeMello[1] and Jennifer A. Bridge[2,*]

Submitted: 06 February 2026 **Accepted:** 23 March 2026 **Publication date:** 10 April 2026

DOI: 10.70465/ber.v3i2.79

Abstract: This paper presents a novel, proof-of-concept, model-free bridge-pier structural assessment framework that can be used to evaluate risk during a storm event or as part of planning exercises. This framework is built on a pre-generated library of bridge-pier failure surfaces—curves that define failure limits for combinations of scour, wind speed, and surge heights—for a range of structural configurations and site conditions. Bridge failure surfaces—generated with basic user inputs—are coupled with real-time storm forecast data to rapidly perform fragility-based risk assessment through Monte Carlo simulations. The resulting fragility curves provide maintenance engineers with actionable information, in the form of estimated failure probabilities, for the bridge of interest as the storm evolves. The results can be combined with real-time scour hole measurements to provide decision support for emergency response as the storm approaches.

The risk assessment framework has been demonstrated on a case study bridge near Cedar Key, Florida, which was in the path of two hurricanes: Ian (2022) and Idalia (2023). The results illustrate how the framework generates fragility curves that are specific to the bridge and the data provided in each storm advisory, without the need to perform detailed finite element analyses. In addition to providing real-time risk assessment, the concepts presented in this paper are also well-suited to performing scenario planning for bridge inventories that may be subject to storm-induced damage. By using historical or projected storm data, bridge vulnerabilities can be explored to inform emergency planning or prioritize bridge maintenance.

Author keywords: Scour; risk assessment; fragility; monitoring; decision support

Introduction

River-crossing and coastal bridges have become more vulnerable to storm-induced demands in the past few decades, with flood-induced scour being one of the leading causes of bridge failures in the United States and China.[1–4] Scour is most often monitored via periodic inspections by trained divers to determine the extent of scour at the time of inspection;[5] however, underwater inspection is not a practical or safe approach to scour risk assessment ahead of and during a storm event. As a storm approaches a region, it is critically important for bridge maintenance engineers to monitor the risk that bridge instability will occur so they can make informed decisions regarding the necessity and timing of bridge closures and to direct post-event structural evaluation for timely return to service.

Approaches to predicting local scour levels either empirically,[6,7] numerically,[8,9] or using emerging machine learning approaches[10,11] provide estimates of maximum scour under constant water velocity; however, these methods have not been applied to provide real-time scour assessment under evolving flow conditions.

Scour hole monitoring devices provide insight into the development of scour holes that may result in pier instability,[12,13] and bridge owners are investing in the installation of hardened wireless scour sensors designed to withstand storm conditions;[14] however, current approaches to risk assessment require scour measurements to be coupled with detailed finite element (FE) models and anticipated wind and storm surge loads. The practicality of performing timely and accurate pier stability risk assessment for bridges located in the path of incoming and potentially damaging storms is limited by the requirements for detailed FE analysis of each bridge and by the uncertainty associated with predicted storm loads. Furthermore, this approach only provides a snapshot of bridge response for a specific combination of scour hole depth and estimated storm-induced loads, without providing information regarding the potential onset of bridge instability for a range of demand combinations from an evolving incoming storm.

Failure surfaces provide a binary evaluation of which combinations of demands (intensity measures) will result in

*Corresponding Author: Jennifer A. Bridge.
Email: jennifer.bridge@essie.ufl.edu
[1]Aon, Boston, MA 02109, USA
[2]Department of Civil and Coastal Engineering, Herbert Wertheim College of Engineering, University of Florida, Gainesville, FL 32611, USA

Discussion period open till six months from the publication date. Please submit separate discussion for each individual paper. This paper is a part of the Vol. 3 of the International Journal of Bridge Engineering, Management and Research (© BER), ISSN 3065-0569.

the structure exceeding a pre-defined limit state, eliminating the need for a full FE analysis. A generalized failure surface—derived from the bridge's geometry and member sizing—is calibrated for a specific site using local soil data. Storm-induced failures predicted by a calibrated failure surface have been shown to align closely with results from bridge-specific FE models, yielding detailed insight into the onset of instability across various scour, wind, and surge combinations.[15]

Fig. 1 shows a failure surface that informs whether a specific bridge has experienced plastic articulation of the pile bents for combinations of wind speed, surge height, and scour hole depth. Combinations of demands that reside above the surface will result in the specified failure.

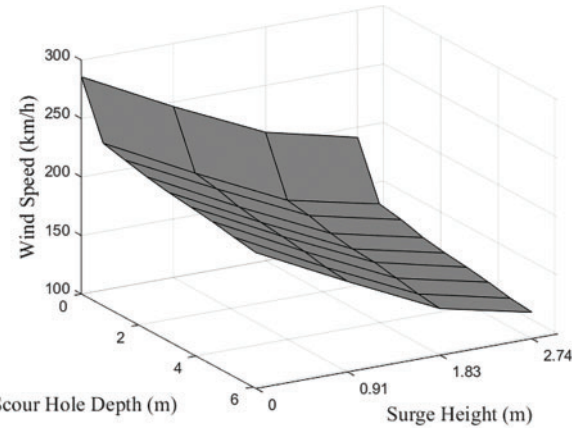

Figure 1. Representative failure surface. Combinations of demand (i.e., wind speed, surge height, and scour hole depth) that lie on or above the surface are considered failure combinations

A library of failure surfaces can be assembled either for a single bridge (covering multiple limit states) or for a class of similar bridges (each surface representing a distinct configuration). To evaluate a particular bridge, a generalized surface is first selected and then adjusted to reflect the site conditions at the bridge. The breadth of the library dictates the library's applicability; it must encompass the design space, demand ranges, and failure criteria relevant to the bridges being evaluated.

For scenario planning, a failure surface library can support risk assessment of individual bridges or entire inventories against storm events. By providing hurricane-specific demand data—from either historical storm records or model outputs from tools such as SLOSH[16] or HWRF[17]—planners can identify vulnerable bridges and develop effective emergency response and maintenance strategies. Examining infrastructure vulnerabilities through planning exercises can help create effective emergency response and maintenance resource allocation plans.[18,19]

Decision support systems (DSS) accelerate hazard response actions.[20,21] Fragility curves, which provide the probability of a structural limit or damage state being exceeded given a measure of demand intensity, have been proposed as a component of DSS for the management of infrastructure subject to natural hazard events.[19,22,23] The research presented herein offers a data-driven decision support tool that builds upon the failure surface concept[15] by developing a methodology for performing fragility-based risk assessment for hurricane-induced failure using National Hurricane Center (NHC) forecast data, real-time scour measurements, and a selected failure surface for the bridge of interest (BoI). The fragility-based risk assessment framework eliminates the need to perform FE modeling of individual bridges and provides near real-time risk assessment tailored to a specific storm forecast in relation to the BoI location.

The novel contribution of this research is a decision support framework that combines: 1) the concept of failure surfaces compiled in a library for rapid "lookup" of demand combinations that result in failure, 2) the near real-time generation of fragility curves for a specific bridge subject to a forecasted storm, and 3) real-time, bridge-located measurements. This paper describes the process for creating a library of failure surfaces and demonstrates how they can be integrated with a probabilistic wind field model and coupled with real-time scour hole and water level measurements to evaluate storm-induced risk. This risk assessment framework is demonstrated for a case study bridge using NHC forecast advisories for Hurricanes Idalia and Ian, producing advisory-specific fragility curves that estimate failure probabilities as the storms evolve. While the case studies presented in this paper were not evaluated with measured data during a storm, this research provides a proof-of-concept that can be built upon in future studies to provide near real-time bridge-safety decision support.

Library of Generalized Failure Surfaces

A bridge class in Florida was selected to illustrate the generation of a library of generalized failure surfaces. The creation of the library requires definition of the parameter space it will represent and analysis of simplified, nonlinear FE models to evaluate responses to a range of projected demands. The selected bridge type—reinforced concrete pile bents with a prestressed concrete superstructure (Fig. 2)—is common in Florida and vulnerable to scour-induced instability during hurricane events. The bridge design and associated parameters were determined following Florida Department of Transportation (FDOT) design guidelines[24] and consultation with FDOT engineers. The American Association of State Highway and Transportation Officials (AASHTO) and Federal Highway Administration design standards[25] were used to supplement FDOT's guidelines where applicable.

The final set of independent parameters defined for the library creation included the pile size, number of piles, beam size, general soil type (represented by the standard penetration test [SPT] blow count, N), initial channel depth, design wind speed for the structure, and demands for scour, wind, and surge, as shown in Table 1.

From these independent parameters, all other variables could be derived, including structural geometry (e.g., deck geometry, bent geometry, pile spacing), modeling parameters (e.g., pile embedment length), and load cases.

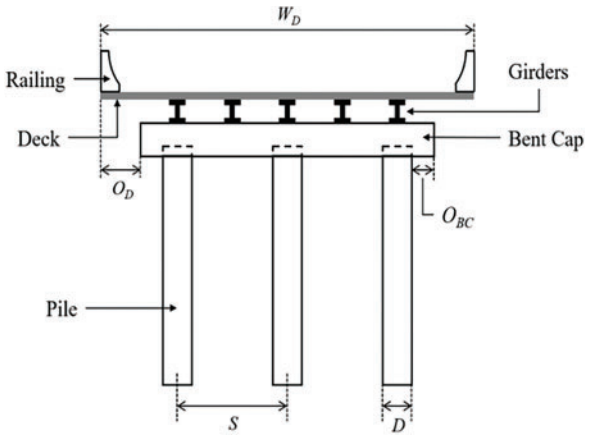

Figure 2. Illustrative drawing of pile bent pier and girder deck superstructure. W_D is deck width, O_D is deck overhang, O_{BC} is bent cap overhang, S is pile spacing, and D is pile size

All FE modeling and analyses were performed using the FB-MultiPier (FB-MP) software package. FB-MP focuses on design-oriented applications and was developed to automatically generate FE models given geometric definitions of the structure and foundation systems. FB-MP analyses couple nonlinear structural FE models with nonlinear soil models to provide robust analysis of bridge piers for axial, lateral, and torsional behaviors. The library generation took advantage of FB-MPs "One Pier Two Span" (OPTS) template and used springs and lumped masses calibrated to equivalently represent multi-pier and multi-span bridges.[26] The OPTS model was previously validated using response data obtained from full-scale bridge-pier barge-collision experiments.[27]

This parameter space resulted in an initial requirement for 201,600 FE models to generate the library. Furthermore, 84 load cases per FE model would be required to represent all possible loading conditions. Two approaches were used to manage the computational expense of creating and analyzing FE models for all combinations of structural parameters and loading conditions. The first approach removed permutations of structural parameters that resulted in unfeasible bridges (e.g., combinations of pile sizes, numbers of piles, and beam spacings that are not allowable or geometrically possible), thus reducing the number of required FE models by 67.6% to 65,290. The second approach focused on decreasing the number of required modeled load cases while still capturing the results of all load combinations. By applying a resultant moment in place of wind and flood loading combinations, only eight distinct load cases were required, resulting in a 90.5% reduction in analysis runtime for a given permutation of structural parameters.[26]

The failure condition considered in the construction of the failure surfaces was lateral failure of the pier in the form of a plastic hinge developed in the bent. Lateral failures have been observed as a leading cause of scour-induced failures in bridge piles, with most lateral failures attributed to the formation of a plastic hinge.[28] Though two plastic hinges are required for collapse, the formation of the first hinge is considered an ultimate limit state in this study. Following the approach in Ahamed, et al.,[5] plastic hinges were considered to have occurred when lateral displacement (in the direction of loadings) at the pile head exceeded a limit-state displacement (Δ_{lim}). To identify Δ_{lim} for each structural permutation, a pushover analysis was performed, where monotonically increasing point loads were applied to the structure and the associated lateral displacement at the pile head was extracted. Once pushover analysis was complete, a force–displacement curve specific to the structural permutation was created, from which Δ_{lim} was extracted.

Python scripts were developed to generate and analyze all FE models, extract output (lateral displacement at pile heads), and plot associated failure surfaces. Fig. 3 is a flowchart illustrating the failure surface library generation procedure.

With a full, generalized failure surface library created, the user can generate a structure-specific failure surface by providing information on the structural configuration and site conditions for the BoI as detailed in DeMello and Bridge:[15] first, a family of failure surfaces that matches the structural

Table 1. Summary of independent variables required to create the library of baseline failure surfaces, upper and lower bounds of parameter range, parameters range increment, and range size

Parameter	Units	Lower bound	Upper bound	Increment	Range size
Pile size	mm	457	762	varies	4
Number of piles	–	3	8	1	6
Beam size	mm	914	1600	229	4
Number of piers	–	1	5	1	5
Soil type	N	10	50	20	3
Initial channel depth	m	1.8	4.6	0.9	4
Design wind speed	m/s	53.6	80.5	4.5	7
Scour hole depth	m	0	6.1	1.5	5
Forecast wind speed	m/s	40.2	89.4	4.5	12
Forecast surge height	m	0.00	5.5	0.9	7

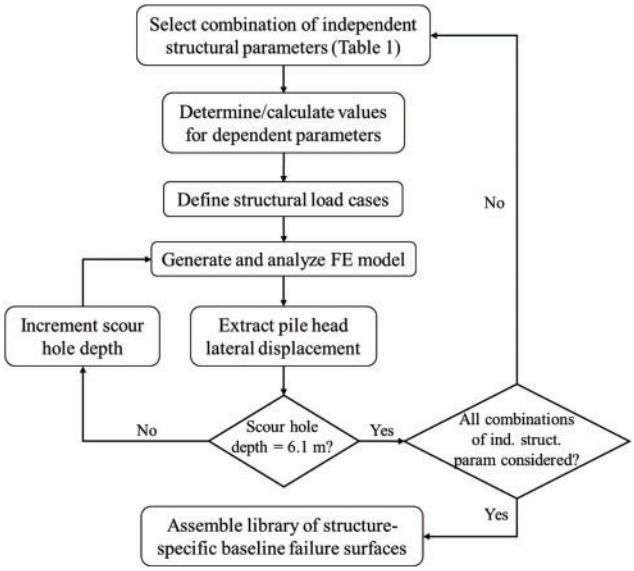

Figure 3. Flowchart illustrating procedure for creating the library of failure surfaces. FE, finite element

configuration is identified, and then a soil homogenization technique, which provides a single SPT blow count surrogate that is representative of the heterogeneous soil profile, is applied to further refine the failure surface for the soil conditions at the site of the bridge.

Fragility-Based Risk Assessment

Once a bridge-specific failure surface has been generated, rapid and model-free risk assessment can be performed when combined with predicted storm-specific demands and measured scour. To estimate predicted wind demands on the BoI's piers given forecast hurricane data, Monte Carlo simulations are performed of a pre-defined wind field model with input values randomly sampled from marginal probability distributions. In this proof-of-concept study, the surge height was considered as a deterministic variable in the risk assessment process since it could either be a measured value as part of a bridge monitoring system or taken as the highest value provided in each forecast range for a conservative risk assessment. A coupled probabilistic representation of surge and wind could be considered in future development of the approach for a more refined, but more computationally demanding, assessment of risk. The results of the current approach are fragility curves—representing the high and low forecasted surge levels—that are specific to a BoI and incoming storm, with scour hole depth as the primary intensity measure.

Real-time assessment is performed considering forecast data for an incoming storm event taken from the NHC's forecast advisories. NHC tracks storms across the Gulf, Atlantic, and Pacific coasts of the United States and publishes advisory reports ("Forecast" and "Public" advisories) every six hours. Advisories contain forecast information on, among other things, the storm's projected track (given as a latitude and longitude pair), central pressure, intensity (maximum sustained and gust wind speeds), and size for eight forecast periods: 0, 12, 24, 36, 48, 72, 96, and 120 hours, with 0 hours being the actual storm data at time of advisory publication.

Wind field model

To determine the failure probability of a bridge pier given a hurricane forecast, information on the failure wind speed and the probability of exceeding the failure wind speed is required. Failure wind speed is taken from the bridge-specific failure curve for a given combination of surge height and scour hole depth. In mathematical form:

$$P_F\,(pier)|FC = P\left(V_{WS} \geq V_{WS,fail}|(SC, SG)\right) \tag{1}$$

where $P_F\,(pier)|FC$ is the probability of pier failure given storm forecast data (FC), V_{WS} is the estimated wind speed at the BoI, $V_{WS,fail}$ is the failure wind speed, SC is the scour hole depth, and SG is the expected surge height taken from the hurricane forecast. Therefore, to calculate the probability of failure (i.e., expected wind speeds exceeding failure wind speeds for a particular forecast), it is necessary to define a wind field model to compute V_{WS} at the BoI.

The Jakobsen and Madsen's site-specific parametric wind field model ("JM model" hereafter) was selected to perform these estimates. The JM model provides estimates of tangential and radial velocity components of wind speeds at 500 m above sea level at a given distance D_R from the storm.[29] A conversion factor of 0.8 is used to convert computed wind speeds from a height of 500 m down to surface (10 m) wind speeds.[30,31] Li and Spence[32] outlined an approach to determine resultant wind speeds at a location of interest considering tangential and radial components from the JM model and the storm's translational speed. However, as was demonstrated by Jakobsen and Madsen, a hurricane's radial component of velocity will be negative due to the pressure differential between the storm's eye and outer regions pulling surrounding air inward. Therefore, resultant wind speeds determined following Li and Spence tend to be lower (yet more representative) than those considering only the tangential component of velocity. To ensure conservatism in the final risk assessment, the framework determines the probability of failure considering only the tangential component of velocity given by:

$$V_{tan} = 0.8V_{max}\left[\sqrt{r'^{-B}\exp\left(1 - r'^{-B}\right) + a^2r'^2} - ar'\right],$$
$$r' = \frac{D_R}{R_{max}},\ a = \frac{fR_{max}}{2V_{max}} \tag{2}$$

where V_{tan} is the tangential velocity at distance D_R from the storm's center, 0.8 is the conversion factor from 500 m to surface, V_{max} is the maximum wind speed, B is Holland's parameter, D_R is the great-circle distance from the storm's center to the location of interest, R_{max} is the radius of maximum winds, f is the Coriolis parameter given by $2\Omega sin(\Psi)$, Ω is the rotation rate of the earth (7.2921 e-5 s^{-1}), and Ψ is the storm's latitude. The inflow angle, α, is defined

as $\tan^{-1}(-V_{rad}/V_{tan})$ and typically has near-surface values between −20° and −25°, resulting in a 6–10% conservative overestimation of the total velocity when using V_{tan}.[33] Fig. 4 is a simple illustration showing V_{tan}, D_R, V_{max}, and R_{max}. Typically, the JM model takes the radius of maximum winds, Holland's parameter, and central pressure deficit (i.e., difference between atmospheric air pressure and the storm's central pressure) as parameters and returns both components of velocity (tangential and radial). The radius of maximum winds and Holland's parameter are presumed known, and central pressure deficit is used to estimate maximum wind speed using:

$$V_{max} = \sqrt{\frac{B\Delta p}{e\rho_a\left(1+\alpha_m^2\right)}} \tag{3}$$

where Δp is the central pressure deficit, e is Euler's number, ρ_a is air density, and α_m is the deflection coefficient.

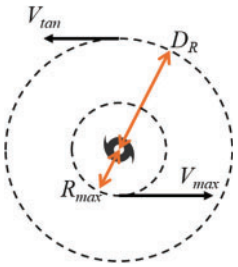

Figure 4. Illustration of V_{tan}, D_R, V_{max}, and R_{max} relative to the hurricane

For application by the framework, however, different input parameters were required due to the data available in NHC's advisory reports. Since NHC already provides estimated maximum sustained and gust wind speeds (both in the present and as forecast), Δp was replaced as input by V_{max}. Furthermore, B and R_{max} are not provided in NHC's advisory reports but can be estimated using information from NHC's advisory reports. For Holland's parameter, the regression fit used by the Florida Public Hurricane Loss Model v5.0 was used:[34]

$$B = 1.74425 - 0.007915\,(\Psi) + 8.4\left(10^{-6}\right)\Delta p + 0.005024(R_{max}) \tag{4}$$

where Δp, the pressure deficit, is given by re-writing Dvorak's fit, Eq. (5), for the North Atlantic data with p_c as the dependent variable.[35,36,37] This approach was chosen because, while NHC provides the central pressure of the storm at present time (i.e., when the advisory is published), it is not part of the forecast data. By re-writing Dvorak's fit, the forecasted maximum wind speed from NHC can be used to determine central pressure at a given forecast period, and by extension Holland's parameter

$$p_c = 1015 - \left(\frac{V_{max}}{3.92}\right)^{1/0.644}\text{(mb)} \tag{5}$$

To determine R_{max}, the procedure outlined by Chavas and Knaff[38] using absolute angular momentum of the storm was used. The procedure uses storm data from NHC advisory reports and relates angular momentum at the outer region of the storm (M_{out}) to the angular momentum at the storm's eye wall (M_{max}). The relationship between R_{max} and R_{out} can then be understood as the fractional loss of angular momentum between outer and inner regions. Therefore, to determine R_{max}, first the angular momentum of the outer region is computed using:

$$M_{out} = R_{out}V_{out} + \frac{1}{2}fR_{out}^2 \tag{6}$$

where R_{out} is the radius to outer region, V_{out} is the velocity in the outer region, and f is the Coriolis parameter. Advisory reports provide information on the storm size as distances from the storm center to regions of threshold wind speeds in four quadrants. Following Chavas and Knaff,[38] R_{out} in the framework is taken as the mean of storm radii associated with 34 kts (62.7 km/h). Following computation of M_{out}, the angular momentum for the inner region (M_{max}) is computed using:

$$M_{max} = M_{out}\,(0.606)\exp\left[\left(-4.84\left(10^{-3}\right)\right)(V_{max}-V_{out}) + \left(-1.44\left(10^{-3}\right)\right)(V_{max}-V_{out})\left(\frac{1}{2}fR_{out}^2\right)\right] \tag{7}$$

where V_{out} is defined as 34 kts (62.7 km/h). Finally, R_{max} is computed using the relationship between M_{out} and R_{max}:

$$R_{max} = \frac{V_{max}}{f}\left(\sqrt{1+\frac{2fM_{max}}{V_{max}^2}}-1\right) \tag{8}$$

where all terms follow prior definitions.

Random variables and associated distributions

Monte Carlo simulations begin with a defined model—numerical, computational, or empirical—and repeatedly sample its inputs from probability distributions. Analysis of the outputs from the randomly sampled inputs can then be performed to extract meaningful insights. To generate realizations of V_{tan}, probability distributions and associated shape parameters for V_{max} and D_R needed to be defined. Furthermore, because the framework was developed to take NHC forecast storm data, it was desirable that the distributions were defined based on NHC model errors.

At the end of every hurricane season, NHC performs model verification studies comparing the forecasted storm data (namely, intensity and track) from their models to available post-storm "best-track" data. NHC then publishes a report summarizing the findings with forecast errors associated with each forecast period.[39] Forecast errors are reported for the year in question and as an average of the errors from the previous 5 years. NHC also provides access to their error database extending back to 1970 for all tracked events.[40] Using the information from NHC's model verifications (database and reports), the probability distribution for V_{max} was assumed Gaussian:

$$V_{max} \sim N\left(V_{max} + \mu_{e,it}, \sigma_{e,it}\right) \tag{9}$$

where $\mu_{e,it}$ and $\sigma_{e,it}$ are mean and standard deviation, respectively, computed from NHC's intensity model error database for a given forecast period. The probability distribution for D_R, however, could not be directly defined since it is a function of the bridge and storm geographical coordinates (latitude and longitude). Therefore, random values for D_R were obtained by randomly sampling track model errors (cross-track and along-track) from NHC's database and calculating D_R for each sampled coordinate pair. Following the approach in Li and Spence, for a given forecast period, cross-track errors were associated with storm latitude ($\Psi_{FC,p}$) and along-track errors were associated with storm longitude ($\lambda_{FC,p}$).[32] Therefore, the probability distribution for cross-track (along-track) was similarly assumed Gaussian:

$$\Psi_{S,p} \sim N\left(\Psi_{FC,p} + \mu_{e,ct}, \sigma_{e,ct}\right) \tag{10}$$

$$\lambda_{S,p} \sim N\left(\lambda_{FC,p} + \mu_{e,at}, \sigma_{e,at}\right) \tag{11}$$

where $\Psi_{S,p}$ and $\lambda_{S,p}$ are sampled latitude and longitude for a given forecast period, $\mu_{e,ct}$ and $\sigma_{e,ct}$ ($\mu_{e,at}$ and $\sigma_{e,at}$) are the mean and standard deviation, respectively, computed from NHC's track model error database for given forecast period. Table 2 provides values used in the framework for μ and σ for intensity, cross-track, and along-track errors for each forecast period.

Failure probabilities

To calculate failure probabilities for a bridge pier in the BoI, the framework performs n Monte Carlo simulations in real time to create n-number of estimated outputs (V_{tan}). As is established, estimates of model output obtained using Monte Carlo simulations become more meaningful (i.e., smaller coefficient of variation [CoV]) with a greater number of model simulations. To determine the approximate number of runs, n, required to obtain a meaningful estimate of failure probabilities, Consolazio et al.[41] presented an approach that uses CoV and an initial estimate of failure probability, given by:

$$n = \frac{1-p}{\delta^2 \cdot p} \approx \frac{1}{\delta^2 \cdot p} \tag{12}$$

where δ is the CoV and p is the initial estimate of failure probability. Values of CoV less than or equal to 0.1 are sufficient for meaningful estimates of failure probabilities.[40] An initial estimate of failure probability, however, is not always known—typically requiring alternative methods to be determined or through additional Monte Carlo simulations. However, because Monte Carlo simulations are not an efficient means of estimating small failure probabilities (i.e., less than 0.01), p was set equal to 0.01 in Eq. (12).[35] Therefore, when performing fragility analysis, the framework samples $n = 10{,}000$ (ten thousand) independent realizations of input parameters, resulting in a random variable vector, $\boldsymbol{V_{tan}}$, containing n number of V_{tan} (bolded variables are used to distinguish between random variables and deterministic single-value variables).

Using $\boldsymbol{V_{tan}}$, failure probabilities are computed as the ratio of the number of model outputs (i.e., V_{tan}) that exceeded the pre-defined limit-state to the total number of input realizations. Expanding on Eq. (1), failure probabilities are calculated using:

$$\begin{aligned} P_F\,(pier)|FC &= P\left(V_{WS} \geq V_{WS,fail}|(SC,SG)\right) \\ &= P\left(V_{tan} \geq V_{WS,fail}|(SC,SG)\right) \\ &= \frac{1}{n}\sum_{i=1}^{n} I(V_{tan,i}) \end{aligned} \tag{13}$$

where n is the number of realizations and $I(V_{tan,i})$ is an indicator function of ith V_{tan}, with the value given by Eq. (14)

$$I\left(V_{tan,i}\right) = \begin{cases} 1, & V_{tan,i} \geq V_{WS,fail} \\ 0, & otherwise \end{cases} \tag{14}$$

Table 2. μ and σ for intensity, cross-track, and along-track error distributions

Forecast period	Intensity		Cross-track		Along-track	
	μ_{it}	σ_{it}	μ_{ct}	σ_{ct}	μ_{at}	σ_{at}
(hrs)	(kts)	(kts)	(deg)	(deg)	(deg)	(deg)
0	−0.2	4.0	0.0167	0.0716	0.0016	0.0883
12	1.7	9.9	0.0000	0.2367	−0.0700	0.2483
24	2.2	13.5	−0.0150	0.3467	−0.1333	0.3867
36	1.9	14.9	0.0000	0.4567	−0.2167	0.5450
48	1.9	15.5	0.0283	0.5900	−0.2816	0.7300
60	1.3	13.7	0.0367	0.6333	−0.1950	0.9083
72	2.5	14.9	0.1283	0.8650	−0.4316	1.2216
96	1.3	15.8	0.2733	1.2200	−0.4500	1.3833
120	−1.5	16.5	0.3483	1.6300	−0.7783	1.9183

Fragility Curves

For a given forecast advisory, the framework begins by evaluating the great-circle distances between the storm's current location, the storm's discrete forecasted locations, and the BoI's location. The framework uses the distances to identify the forecasted storm locations (separated by six hours) closest to the BoI, and their respective forecast periods. Using storm location coordinates, vector algebra is performed to find the coordinate pair nearest the BoI, $(\tilde{\Psi}, \tilde{\lambda})$, that lies on the segment between the two identified storm forecast locations. If the distance between the BoI and the nearest point, $D(\tilde{\Psi}, \tilde{\lambda})$, is less than the distances from the BoI to the identified storm forecast locations, $D\left(\Psi_{FC,Pi}, \lambda_{FC,Pi}\right)$, then the new point is selected by the framework as the storm location to be used in the assessment. Fig. 5 provides an illustrative example showing three forecasted storm locations, distances to the two forecast locations nearest the BoI (star in the figure), and the distance to the point nearest the BoI on the forecasted track.

Figure 5. Illustrative example showing different forecast locations, distances between BoI and forecasted locations, position on forecasted track nearest BoI, and distance to nearest point

By re-positioning the storm to the point on its projected path nearest to the BoI, the framework can better handle situations where the BoI lies between the two nearest forecast periods. When the BoI is between two forecast period locations, it is possible to obtain a null fragility curve (i.e., 0% probability of failure for all damage states) if the distance between the bridge and forecasted storm locations is large enough. This occurs because the JM model appropriately returns low wind velocities when the point of reference is far away from the storm's center. Therefore, when performing fragility analysis, the framework would compute zero probability of failure despite forecasted track indicating that the storm is expected to directly impact the bridge. By re-positioning the storm to the nearest point, computed distances between the storm's eye and the bridge are only ever large when the storm track itself is far from bridge (i.e., storm not expected to directly impact the bridge). This allows the framework to conservatively perform fragility analysis by simply moving the worst of the two identified forecasts (i.e., the one with the higher forecasted maximum wind speeds) to the point on the forecasted track nearest the BoI. Furthermore, this approach does not require additional forecast modeling for storm data at the new (re-positioned) coordinates. If the distance to the nearest point matches the distance to either of the identified forecast periods, then no re-positioning is required, and the framework selects the storm data associated with the forecast period that is nearest the bridge. Fig. 6 is a flowchart summarizing the procedure to identify which storm forecast data to use in the fragility analysis.

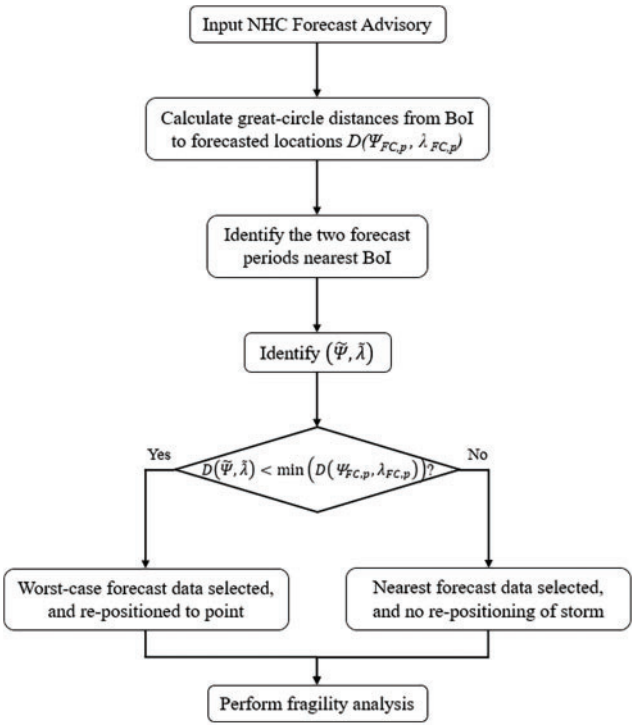

Figure 6. Flowchart of procedure to select storm data for fragility analysis. NHC, National Hurricane Center

Having identified which forecast period and associated storm data to use, the framework independently samples a value for V_{max}, $\Psi_{FC,p}$, and $\lambda_{FC,p}$ from their respective distributions (Eqs. (9)–(11)) and passes the sampled values as inputs into the JM model. Using the bridge-specific failure surface along with a forecasted range of surge heights, the framework defines $V_{WS,fail}$ for each increment of scour hole depth. Then failure probabilities are computed for each increment of scour hole depth and plotted against scour hole depths to generate bridge- and forecast advisory-specific fragility curves. Fig. 7 is a flowchart summarizing the procedure used by the framework to compute failure probabilities.

Risk Assessment Demonstration

Once the framework generates the failure surface associated with a given BoI, the framework performs fragility-based

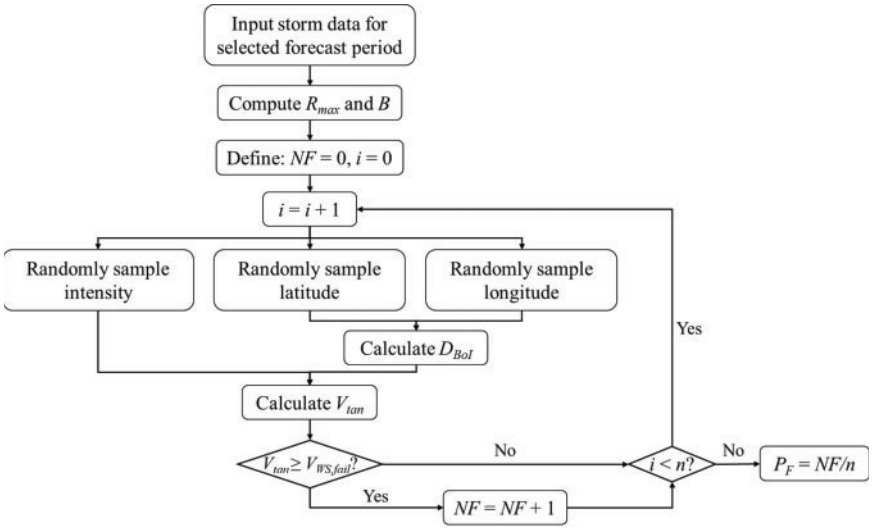

Figure 7. Flowchart of fragility analysis procedure performed by framework

risk assessment using input hurricane data (forecasted or simulated) and Monte Carlo simulations to provide maintenance engineers with fragility curves—probabilities of failure associated with a range of scour values for a specific storm advisory. The time to perform risk assessment considering 10,000 Monte Carlo simulations was measured to be eight minutes on average per advisory using a 3-GHz (4.6 GHz peak) CPU with 18 cores, 128 GB (4 × 32 GB) of DDR4 RAM, and a Polaris 23 GPU. If a larger inventory of bridges requires assessment as a storm approaches, a parallelized computing approach could be adopted to ensure the total runtime remains low enough for timely decision support.

The demonstration presented herein is an application of the risk assessment procedure to the S.R. 24 bridge in Cedar Key, Florida. This bridge is one of three bridges covering the parameter space provided in Table 1 and was previously used to validate the failure surface approach to response prediction.[15] This bridge was selected because of its proximity to the path of two recent hurricanes, representing a realistic condition for the application and demonstration of the risk assessment framework developed in this research. The 110-m-long bridge, located on the Gulf coast in central Florida, crosses the marshlands into Cedar Key and has seven interior piers (i.e., located within the channel) comprised of five 0.46-m square piles that support a two-way road (i.e., one lane in each direction). The soil at the site is fairly homogeneous with medium cohesionless soil. Fragility curves were generated using failure surfaces associated with S.R. 24 and historical NHC advisory reports (forecasts) for Hurricanes Idalia and Ian.

Hurricane Idalia

Idalia was a powerful storm that made landfall near Keaton Beach, Florida (approximately 96.6 km from Cedar Key) as a strong Category 3 hurricane (201.2 km/h maximum sustained wind speeds) in August 2023. It was a highly destructive hurricane, bringing devastating surges of 2.1 to 3.7 m across the northwestern coast of Florida, including Cedar Key. NHC's first advisory report was published on August 26, 2023; however, for the presented demonstration, fragility curves were created using forecast advisories 10 through 15. These advisories were selected because they demonstrate the evolution of the storm's track and capture hurricane conditions from approximately 48 hours before landfall up to the time of landfall.

Beginning with forecast advisory 10, the framework computes distances between the BoI and each forecasted location, $D\left(\Psi_{FC,Pi}, \lambda_{FC,Pi}\right)$, to identify the two forecast period locations nearest to the BoI. Fig. 8 is a modified version of NHC's graphical representation of the forecasted track presented in forecast advisory 10. FC_{Pi} in the figure indicates the forecast period associated with each forecasted location (e.g., FC_{P0} is the forecast of the storm at the time the advisory is issued, FC_{P12} is the forecast for the storm 12 hours from the time of the advisory, etc.). The highlighted forecast periods (orange box) are the two forecast locations nearest the BoI. The framework then computes the distance to the nearest point, $D\left(\tilde{\Psi}, \tilde{\lambda}\right)$, on the projected track connecting FC_{P36} and FC_{P48}. Since $D\left(\tilde{\Psi}, \tilde{\lambda}\right)$ is less than $D\left(\Psi_{FC,P36}, \lambda_{FC,P36}\right)$—82.4 km and 111 km, respectively—the framework re-positions FC_{P36} to the geographical coordinates $\tilde{\Psi}, \tilde{\lambda}$ and begins the fragility assessment.

Assessment begins by sampling n number of independent realizations of V_{max}, Ψ_S, and λ_S using Eqs. (9)–(11), respectively. Furthermore, because the storm was re-positioned, $\Psi_{FC,P}$ and $\lambda_{FC,P}$ in Eqs. (10) and (11), were replaced with $\tilde{\Psi}, \tilde{\lambda}$. The statistics used to define the marginal distributions were taken from Table 2 for the given forecast period (i.e., FC_{P36}). The sampled values are then passed into the JM model to define V_{tan} (i.e., the random variable of estimated

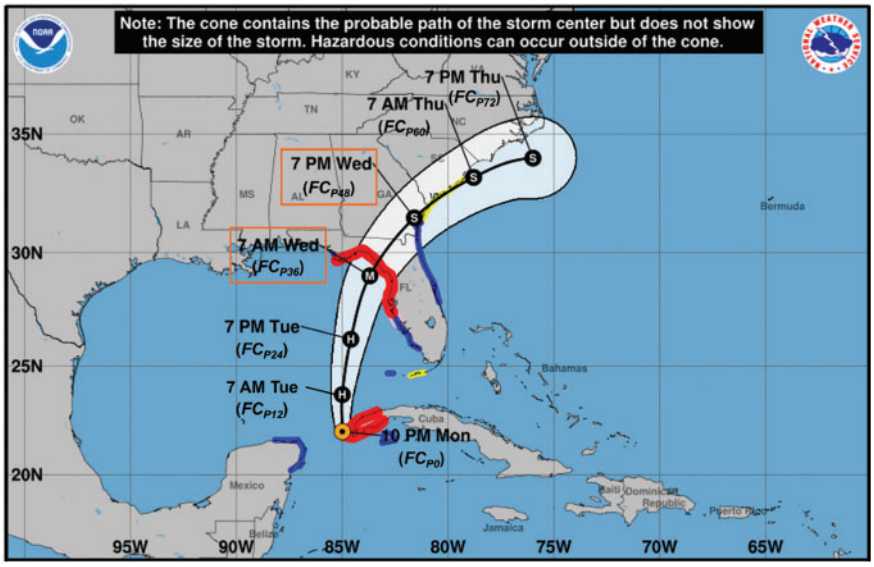

Figure 8. A modified version of NHC's graphical representation of the forecasted track of Hurricane Idalia presented in forecast advisory 10. Orange boxes highlight the two forecast periods nearest the BoI (yellow star). NHC, National Hurricane Center

wind speeds at the BoI) following the procedure described earlier. Furthermore, because NHC does not publish forecast model errors associated with surge height forecasts, surge heights are considered deterministically, and assessment is performed leveraging bridge-specific failure curves associated with the input surge height.

From advisory 10, the forecasted storm surge at Cedar Key ranged from 1.83 m to 3.66 m. Therefore, values of $V_{WS,fail}$ for each increment of scour hole depth were taken from the bridge-specific failure curves associated with 1.83 and 3.66 m surge, respectively. Fig. 9a shows the generalized failure curves for 1.83 and 3.66 m surge, and Fig. 9b shows the fragility curves obtained from each failure curve.

Fig. 10 shows the fragility curves for forecast advisories 10 through 15. Table 3 is a summary of the forecast period and data used to generate fragility curves for each advisory. For ease of readability, only the fragility curves associated with the upper bound of the forecasted surge heights are shown.

NHC's forecast advisories for Hurricane Idalia presented consistent intensity forecasts after advisory 10, when the upper bound of forecasted surge dropped from 3.66 to 3.05 m. As a result, the greatest difference between each subsequent advisory was the storm's position relative to the BoI. As subsequent advisories (11 through 15) were published, it became evident that Idalia was veering away from the BoI. This can be seen in Fig. 10 with failure probabilities decreasing as more advisory reports were published. Furthermore, according to the results presented in Fig. 10, S.R. 24 presented no significant risk of failure at the time of landfall (advisory 15), regardless of scour hole depth. Following Idalia's passage, FDOT inspected and subsequently re-opened S.R. 24 within 12 hours of landfall, lending some merit to the framework's performance.

Table 2 summarizes the results of the analyses conducted for advisories 10 to 15, showing the evolution of the projected wind velocities, distance of the projected track to the BoI, and the probability of failure for no scour and 1.52 m of scour. The highest probability of failure is given at the earliest assessed advisory (advisory 10) when the projected storm is three days from the BoI: a 25% probability of failure is estimated for the projected storm conditions with just over 3 m of surge and 1.52 m of scour.

Hurricane Ian

Ian made landfall in southwestern Florida as a Category 4 hurricane in September 2022, producing devastating storm surges and winds (249.5 km/h maximum sustained wind speeds) and causing historic freshwater flooding across much of central and northern Florida. Ian differed from Idalia in that, as it neared the Florida coast, it significantly slowed down, resulting in the close proximity of subsequent forecast locations. The presented fragility curves (Fig. 11) were created using forecast advisories 14 through 19. Like Idalia, these advisories were selected because they demonstrate the evolution of the storm's track and capture hurricane conditions starting approximately 72 hours before landfall. The selected advisory reports do not capture hurricane conditions at landfall because, by the time Ian made landfall, the forecasted track had turned away from the BoI.

Fig. 11 presents the fragility curves for the selected forecast advisories using failure curves generated from input structural parameters for S.R. 24. Only fragility curves associated with the upper bound of forecasted surge heights are shown. From Fig. 11 it can be observed how failure

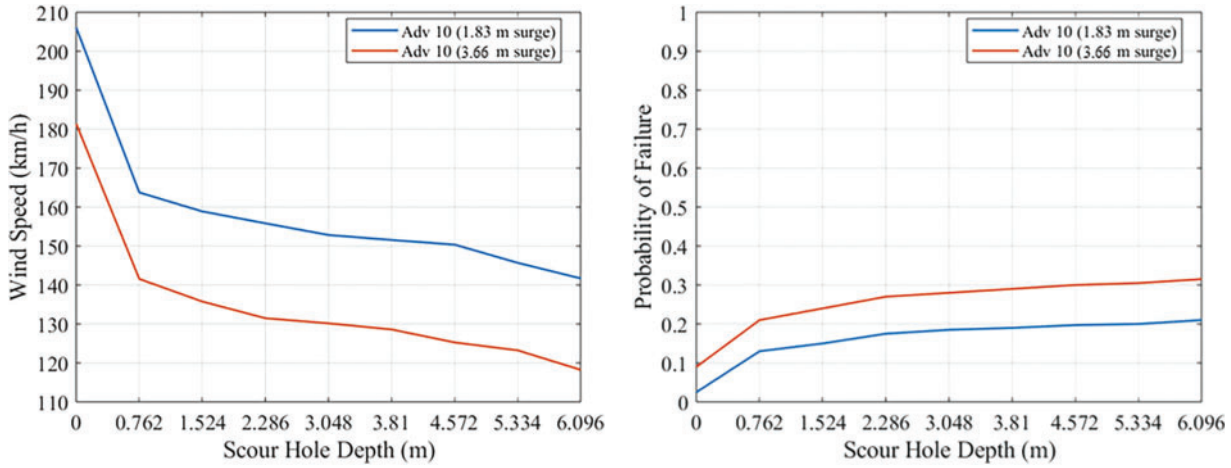

(a) (b)

Figure 9. Outputs from the framework using input structural parameters for S.R. 24 and forecast storm data from NHC's forecast advisory 10 for Hurricane Idalia. (a) Failure curves for 1.83 and 3.66 m surge and (b) fragility curves obtained from each failure curve for the same advisory

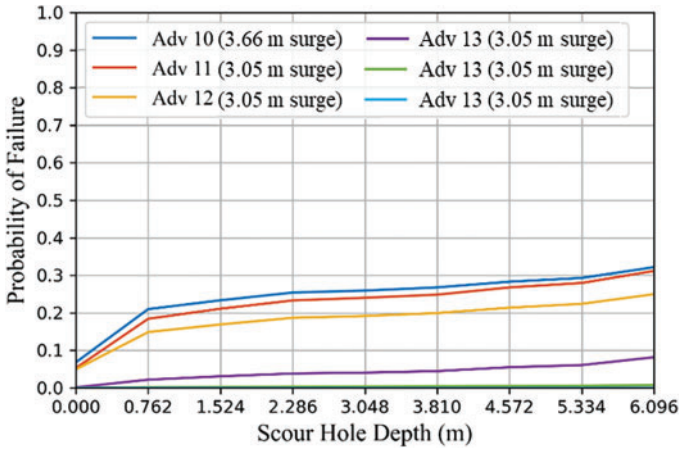

Figure 10. Fragility curves for various Hurricane Idalia advisory reports. Fragility curves were generated using the upper bound of forecasted surge heights

Table 3. Summary of forecasted storm data for Idalia advisories. FC_P is selected forecast, V_{WS} is forecasted maximum gusts, D_{BoI} is distance from BoI to forecasted storm location, SG is maximum forecasted surge height, $P_{F,0}$ and $P_{F,5}$ are failure probabilities for 0 and 1.52 m scour, respectively

Adv Num	FC_P	V_{WS}	D_{BoI}	SG	$P_{F,0}$	$P_{F,5}$
	(hrs)	(km/h)	(km)	(m)		
10	36	241.4	68.9	3.66	0.08	0.25
11	24	241.4	194.5	3.05	0.06	0.21
12	24	249.4	71.5	3.05	0.06	0.16
13	12	225.3	171.3	3.05	0.00	0.04
14	12	257.5	132.7	3.05	0.00	0.00
15	0	257.5	101.3	3.05	0.00	0.00

probabilities increase as NHC forecasts Ian approaching the BoI. The procedure captures the slowdown of Ian from forecast advisory 15 to 16, resulting in a decrease in failure probability due to Ian losing intensity in this period. Failure probabilities increase once more for forecast advisory 17 as the storm begins moving again and gains strength. However,

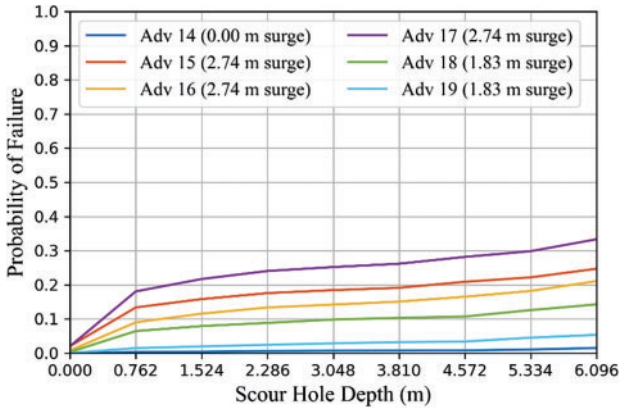

Figure 11. Fragility curves for various Hurricane Ian advisory reports. Fragility curves were generated using the upper bound of forecasted surge heights, shown in parentheses

as Ian turns east, away from the BoI, failure probabilities drop once more until the BoI is out of Ian's area-of-effect. A summary of the forecast data is presented in Table 4.

Discussion and Guidelines for Applications

By leveraging a library of failure surfaces generated prior to deployment and the presented risk assessment procedure, the framework can quickly perform real-time or scenario hazard planning structural assessment for a number of bridges that may be impacted by storm events. Real-time assessment is carried out by coupling real-time scour hole depth measurements with storm forecast data from NHC for an incoming storm. For a given bridge and forecast advisories specific to the incoming storm, maintenance engineers can quickly obtain fragility curves with scour hole depth as the primary intensity measure. If available, real-time scour measurements can then be used to identify the probability of failure for the incoming storm and inform the likelihood of sustained damage during the event. To use the output of this framework for decision support, bridge engineers and emergency responders will need to establish a failure probability threshold that dictates if and when a bridge should be closed to traffic; this threshold may depend on how far the storm is from impacting the bridge and how critical the bridge is for evacuation, among other factors. Even after closing the bridge, a rising probability of failure will indicate a higher likelihood of damage requiring post-storm assessment and repairs.

Scenario hazard planning can be performed with projected (or measured) scour hole depths and simulated storm data. Output fragility curves provide maintenance engineers with granular information regarding the onset of pier instability given a range of demand combinations. Scenario hazard planning allows for regional assessment of a suite of bridges (within the framework's scope of applicability), allowing engineers to design emergency evacuation routes that are robust to specific storm conditions.

It is important to note that the framework's scope of application is limited to the scope of the pre-generated library of failure surfaces; the framework, as presented, should only be applied to pile bent pier designs with driven square reinforced concrete piles supporting girder deck superstructures crossing navigable waterways.

Recommendations for Future Work

The proof-of-concept risk assessment framework set surge levels as a deterministic variable, rather than using a probabilistic model that coupled surge with wind speeds. Future work should evaluate how such a coupled model would impact the results and determine whether the additional computational expense would be warranted.

The modeling used in the generation of the failure surfaces assumes the structure is performing as intended, without accounting for possible deterioration or defects, other than scour. Future research may consider incorporating bridge condition assessment information to update the failure surface to reflect changes in capacity. In addition, the presented risk assessment framework is designed to be data-driven, with scour hole measurements available from the bridge before and during the storm impact. This requires robust and environmentally hardened instrumentation, installation, and communication hardware.

Table 4. Summary of forecasted storm data for Ian advisories. FC_P is selected forecast period, V_{WS} is forecasted maximum gusts, D_{BoI} is distance from BoI to forecasted storm location, SG is maximum forecasted surge height, $P_{F,0}$ and $P_{F,5}$ are failure probabilities for 0 and 1.52 m scour, respectively

Adv num	FC_P	V_{WS}	D_{BoI}	SG	$P_{F,0}$	$P_{F,5}$
	(hrs)	(km/h)	(km)	(m)		
14	72	201.2	123.9	0	0.00	0.00
15	72	169.0	111.6	2.74	0.02	0.17
16	72	144.8	80.7	2.74	0.01	0.12
17	60	169.0	118.3	2.74	0.02	0.22
18	48	169.0	144.0	1.83	0.00	0.07
19	36	160.9	160.7	1.83	0.00	0.02

A full-scale, real-time application of this framework on several bridges instrumented for scour in a hurricane-prone region would provide a validation opportunity and drive improvements to ensure it is an effective decision support tool for bridge engineers.

Conclusions

This study presents a procedure for rapidly performing fragility-based risk assessment for bridges vulnerable to storm-induced scour damage. This novel approach to evaluating storm forecast-specific failure probability is achieved by coupling a pre-generated library of generalized failure surfaces with a risk assessment procedure that uses rapid Monte Carlo simulation of the JM model to estimate wind speeds at the bridges of interest. The assessment framework provides maintenance engineers with actionable information—in the form of fragility curves—regarding a bridge's risk to input storm data without requiring additional FE modeling.

The risk assessment procedure was demonstrated using a real case study bridge (S.R. 24 in Cedar Key, Florida) that had the potential to be impacted during two recent hurricanes (Ian in 2022 and Idalia in 2023). The results of the demonstration illustrate how fragility curves rapidly generated by the framework in response to each hurricane advisory can capture changes to a bridge's risk due to changes in the storm's forecasted track and intensity as it develops. Real-time scour measurements coupled with storm-specific failure probabilities provide bridge engineers with actionable information to support bridge closure and post-storm action decision making.

Data Availability Statement

Framework output data is available upon request to the authors. All national hurricane center forecast data is publicly available at https://www.nhc.noaa.gov.

Acknowledegments

The research presented in this paper was funded in part by the united states national science foundation, cmmi-1452911. The opinions, findings, and conclusions expressed in this publication are those of the author(s).

References

[1] Wardhana K, Hadipriono FC. Analysis of recent bridge failures in the United States. *J Perform Construct Facil*. 2003;17(3):144–150. doi:10.1061/(ASCE)0887-3828(2003)17:3(144).

[2] Lagasse PF, Smith T, Wang J, Chen L. *Hydraulic Engineering Circular 20 (HEC-20): Stream Stability at Highway Structures*. 4th edition, FHWA-HIF-12-004. FHWA, U.S. Department of Transportation. https://www.fhwa.dot.gov/engineering/hydraulics/pubs/hif12004.pdf.

[3] Xion W, Cai CS, Zhang R, Shi H, Xu C. Review of hydraulic bridge failures: historical statistic analysis, failure modes, and prediction methods. *J Bridge Eng*. 2023;24(4). doi:10.1061/JBENF2.BEENG-5763.

[4] Zhang G, Liu Y, Liu J, Lan S, Yang J. Causes and statistical characteristics of bridge failures: a review. *J Traff Trans Eng (Engl. Ed.)*. 2022;9(3):388–406. doi:10.1016/j.jtte.2021.12.003.

[5] Ahamed T, Duan JG, Jo H. Flood-fragility analysis of instream bridges–consideration of flow hydraulics, geotechnical uncertainties, and variable scour depth. *Struct Infrast Eng*. 2020;17(11):1494–1507. doi:10.1080/15732479.2020.1815226.

[6] Melville BW, Sutherland AJ. Design method for local scour at bridge piers. *J Hydra Eng*. 1988;114(10). doi:10.1061/(ASCE)0733-9429(1988)114:10(1210).

[7] Briaud JL. Scour depth at bridges: method including soil properties. I: maximum scour depth prediction. *J Geotech Geoenviron Eng*. 2014;141(2):04014104. doi:10.1061/(ASCE)GT.1943-5606.0001222.

[8] Lai YG, Liu X, Bombardelli FA, Song Y. Three-dimensional numerical modeling of local scour: a state-of-the-art review and perspective. *J Hydra Eng*. 2022;148(11):0312202. doi:10.1061/(ASCE)HY.1943-7900.0002019.

[9] Olsen NR, Kjellesvig HM. Three-dimensional numerical flow modeling for estimation of maximum local scour depth. *J Hydra Res*. 1998;36(4):579–590. doi:10.1080/00221689809498610.

[10] Choi SU, Choi B, Lee S. Prediction of local scour around bridge piers using the ANFIS method. *Neural Comput Applicat*. 2017;28(2):335–344. doi:10.1007/s00521-015-2062-1.

[11] Kim T, Shahriar AR, Lee W-D, Choi Y, Kwon S, Gabr MA. Field data-based prediction of local scour depth around bridge piers using interpretable machine learning. *Transport Geotech*. 2025;52(4):101567. doi:10.1016/j.trgeo.2025.101567.

[12] Brandimarte L, Paron P, Di Baldassarre G. Bridge pier scour: a review of processes, measurements and estimates. *Environ Eng Manag J*. 2012;11(5):975–989. doi:10.30638/eemj.2012.121.

[13] Prendergast LJ, Gavin K. A review of bridge scour monitoring techniques. *J Rock Mech Geotech Eng*. 2014;6(2):138–149. doi:10.1016/j.jrmge.2014.01.007.

[14] Resensys. Scour-critical bridges monitoring in Florida FDOT and quick assessment after hurricanes. *Resensys Blog*. 2025. Accessed January 14, 2026. https://www.resensys.com/Blog/project/scour-critical-bridges-monitoring-in-florida-fdot-and-quick-assessment-after-hurricanes/.

[15] DeMello N, Bridge JA. A generalized, model-free framework for assessing scour-induced bridge pier instability. *Eng Struct*. 2024;309(3):309. doi:10.1016/j.engstruct.2024.118086.

[16] Jelesnianski CP, Chen J, Shaffer WA. SLOSH: Sea, Lake, and Overland Surges from Hurricanes. NOAA Technical Report NWS 48. National Oceanic and Atmospheric Administration, U.S. Department of Commerce; 1992;1–71. https://repository.library.noaa.gov/view/noaa/7235.

[17] Gopalakrishnan SG, Liu Q, Marchok T, et al. Hurricane weather research and forecasting (HWRF) model scientific documentation. *Development Testbed Center*. 2010;75. https://www.aoml.noaa.gov/ftp/hrd/gopal/BOULDER_2010/HWRF_final_2-2_cm-1.pdf.

[18] Clarke J, O'Brien EA. Multi-hazard risk assessment methodology, stress test framework and decision support tool for resilient critical infrastructure. *Trans Res Procedia*. 2016;14:1355–1363. doi:10.1016/j.trpro.2016.05.208.

[19] Bachmann D, Huber NP, Johann G, Schüttrumpf H. Fragility curves in operational dike reliability assessment. *Georisk: Assess Manag Risk Eng Syst Geohaz*. 2013;7(1):49–60. doi:10.1080/17499518.2013.767664.
[20] Wallace WA, De Balogh F. Decision support systems for disaster management. *Public Administ Rev*. 1985;45:134–146. doi:10.2307/3135008.
[21] Tufekci S. An integrated emergency management decision support system for hurricane emergencies. *Safety Science*. 1995;20(1):39–48. doi:10.1016/0925-7535(94)00065-B.
[22] Giovinazzi S, Pollino M, Rosato V, Clemente P, Buffarini G. A decision support system for the emergency management of highways in the event of earthquakes. Atti del XVIII Convegno ANIDIS L'ingegneria Sismica in Italia: Ascoli Piceno; 2019:101–110. https://iris.enea.it/handle/20.500.12079/61773
[23] Kameshwar S, Cox DT, Barbosa R, Farokhnia K, Park H, Alam MS, van de Lindt JW. Probabilistic decision-support framework for community resilience: Incorporating multi-hazards, infrastructure interdependencies, and resilience goals in a Bayesian network. *Reliab Eng Syst Saf*. 2019;191(4):106568. doi:10.1016/j.ress.2019.106568.
[24] FDOT. FDOT design manual. Florida Department of Transportation, Tallahassee, FL; 2018. https://www.fdot.gov/docs/default-source/roadway/fdm/current/2018FDM260BridgeStruct.pdf.
[25] AASHTO. *AASHTO LRFD Bridge Design Specifications*. Washington, DC: American Association of State and Highway Transportation Officials; 2012.
[26] DeMello N. A generalized model-free framework for assessing scour-induced bridge pier instability. Ph.D. dissertation, University of Florida, Gainesville; 2024. https://ufdc.ufl.edu/ufe0061018/00001.
[27] Consolazio GR, Davidson MT. Simplified dynamic analysis of barge collision for bridge design. *Transp Res Rec: J Trans Res Board*. 2008;2050(1):13–25. doi:10.3141/2050-02.
[28] Lin C, Han J, Bennett C, Parsons RL. Case history analysis of bridge failures due to scour. *Climatic Eff Pavem Geotechn Infrastruct*. 2014: 204–216. doi:10.1061/9780784413326.021.
[29] Jakobsen F, Madsen H. Comparison and further development of parametric tropical cyclone models for storm surge modeling. *J Wind Eng Indust Aerodyn*. 2004;92(5):375–391. doi:10.1016/j.jweia.2004.01.003.
[30] Powell MD. Evaluations of diagnostic marine boundary-layer models applied to hurricanes. *Monthly Weather Rev*. 1980;108(6):757–766. doi:10.1175/1520-0493(1980)108<0757:EODMBL>2.0.CO;2.
[31] Powell MD, Vickery PJ, Reinhold TA. Reduced drag coefficient for high wind speeds in tropical cyclones. *Nature*. 2003;422:279–283. doi:10.1038/nature01481.
[32] Li B, Spence SM. Real-time forecast of hurricane-induced damage risk to envelope systems of engineered buildings through metamodeling. *J Wind Eng Indust Aerodyn*. 2023;232(2):105273. doi:10.1016/j.jweia.2022.105273.
[33] Zhang JA, Uhlhorn EW. Hurricane sea surface inflow angle and an observation-based parametric model. *Monthly Weather Rev*. 2012;140(11):3587–3605. doi:10.1175/MWR-D-11-00339.1.
[34] Oxenyuk V, Gulati S, Kibria BM, Hamid S. Distribution fits for various parameters in the florida public hurricane loss model. *J Modern Appl Statist Meth*. 2017;16(1):481–497. doi:10.56801/10.56801/v16.i.908.
[35] Dvorak VF. Tropical cyclone intensity analysis and forecasting from satellite imagery. *Month Weather Rev*. 1975;103(5):420–430. doi:10.1175/1520-0493(1975)103.
[36] Dvorak VF. Tropical cyclone intensity analysis using satellite data. NOAA Technical Reports; 1984. https://repository.library.noaa.gov/view/noaa/19322/noaa_19322_DS1.pdf.
[37] Holland B. A revised hurricane pressure–wind model. *Monthly Weather Rev*. 2008;136(9):3432–3445. doi:10.1175/2008MWR2395.1.
[38] Chavas D, Knaff JA. A simple model for predicting the tropical cyclone radius of maximum wind from outer size. *Weath Forecast*. 2022;37(5):563–579. doi:10.1175/WAF-D-21-0103.1.
[39] National Hurricane Center. Verification of the NHC Forecasts for the 2022 Hurricane Season; 2022, https://www.nhc.noaa.gov/verification/pdfs/Verification_2022.pdf.
[40] National Hurricane Center. National Hurricane Center Forecast Verification; 2025. https://www.nhc.noaa.gov/verification/verify7.shtml.
[41] Consolazio GR, Davidson MT, Getter JD. Vessel crushing and structural collapse relationships for bridge design. FDOT Technical Report 2010. https://www.impact.essie.ufl.edu/wp-content/uploads/sites/176/2020/08/UF-report-2010-72908-74039.pdf.